Front. Optoelectron. 2012, 5(1): 82–89
DOI 10.1007/s12200-012-0194-9

RESEARCH ARTICLE

High speed optical modulation in Ge quantum wells using quantum confined stark effect

Yiwen RONG[1], Yijie HUO (✉)[1], Edward T. FEI[1], Marco FIORENTINO[2], Michael R.T. TAN[2], Tomasz OCHALSKI[3], Guillaume HUYET[3], Lars THYLEN[4], Marek CHACINSKI[4], Theodore I. KAMINS[1], James S. HARRIS[1]

1 Department of Electrical Engineering, Stanford University, Stanford, CA 94305, USA
2 Quantum Science Research, Hewlett-Packard Laboratories, Palo Alto, CA 94304, USA
3 Tyndall National Institute, Lee Maltings, Photonics Building, Cork, Ireland
4 Photonics and Microwave Engineering Royal Institute of Technology Kista, Stockholm S-164 40, Sweden

© Higher Education Press and Springer-Verlag Berlin Heidelberg 2012

Abstract We focus on the optimization of SiGe material deposition, the minimization of the parasitic capacitance of the probe pads for high speed, low voltage and high contrast ratio operation. The device fabrication is based on processes for standard Si electronics and is suitable for mass-production. We present observations of quantum confinement and quantum-confined Stark effect (QCSE) electroabsorption in Ge quantum wells (QWs) with SiGe barriers grown on Si substrates. Though Ge is an indirect gap semiconductor, the resulting effects are at least as clear and strong as seen in typical III–V QW structures at similar wavelengths. We also demonstrated a modulator, with eye diagrams of up to 3.5 GHz, a small driving voltage of 2.5 V and a modulation bandwidth at about 10 GHz. Finally, carrier dynamics under ultra-fast laser excitation and high-speed photocurrent response are investigated.

Keywords electroabsorption effect, Ge, optical interconnections, optical modulators, quantum-confined Stark effect (QCSE), Ge/SiGe quantum wells (QWs)

1 Introduction

Quantum-confined Stark effect (QCSE) [1,2] is a strong optical absorption that has been observed in several groups of quantum well (QW) materials. The QCSE is used extensively for high-speed [3], low power dissipation optical modulators, for example, in telecommunications, and as well as in large arrays of low power devices [4]. QCSE has been used extensively in III–V semiconductor QW structures, such as GaAs/AlGaAs, InGaAs/InP, AlGaAs/AlAs [5–10]. In group IV alloys, we previously demonstrated the QCSE in Ge QW with SiGe barriers [11,12]. The group IV QW structures have the potential to operate at low power and therefore enable the applications for on-chip optical interconnect and fully integrated modulators for optical telecommunications [13–15]. These devices show clear QCSE whose performance is comparable to, or possibly better than, III–V QCSE effects at similar wavelengths. In the paper, we discussed the material growth, device fabrication and characterization of the high-speed modulator.

2 Band structure and sample design

Both Si and Ge are indirect bandgap materials. Though the maximum in the valence band is at the zone center (zero effective momentum), the global minima in the conduction band of Si and Ge are not at the zone center. The valence band maxima and the conduction band minima are not at the same effective momentum, thus optical transitions between the valence band maxima and conduction band minima are indirect. This requires phonons so that the effective momentum can be conserved, because the photon momentum is negligible on this scale.

While Ge has a weak, indirect optical absorption tail extending almost to 2 μm (0.62 eV) at room temperature [16], it also has a strong and abrupt rising absorption edge at 1.55 μm wavelength (0.8 eV) [17–19]. This strong edge corresponds to the direct optical absorption at the zone center. The band structure of the zone center minimum and of the zone-center valence band maxima is similar to that

Received September 16, 2011; accepted November 7, 2011

E-mail: yijiehuo@gmail.com

of direct gap materials like GaAs, and thus behaves very similarly, obeying the same models, such as the Kane k▪p model [19] that gives the basic scaling of optical absorption strength with bandgap energy. Hence, we expect this direct optical absorption to behave similarly to that in direct gap semiconductors like GaAs, though with an additional, weak indirect absorption tail extending to lower photon energies.

Figure 1 shows the basic structure in our experiments. It is similar to our previous work [11,12]. The relaxed buffer layer used a low temperature growth and high temperature annealing technique to optimize the surface roughness and the dislocation densities of the buffer layer. This improves the material and optical quality of the QW region. $Si_{0.1}Ge_{0.9}$ has a larger lattice constant than Si. Our sample balances the strain between the wells and the barriers by setting the average of the Si concentration in the supper lattice QW region equal or close to that of the buffer layer.

Figure 2 illustrates the physics behind the QCSE. When a semiconductor is fabricated with very thin layers (e.g., 10 nm), the optical absorption spectrum changes radically as a result of the quantum confinement of carriers in the 1D QWs. When there is no electric field (E-field), electron and hole wavefunctions are confined in the QW, and the overlap of the wavefunctions is increased. These results in an increase in the oscillator strength of the interband transitions between the discrete electron and hole bound energy states, which are produced by the size quantization.

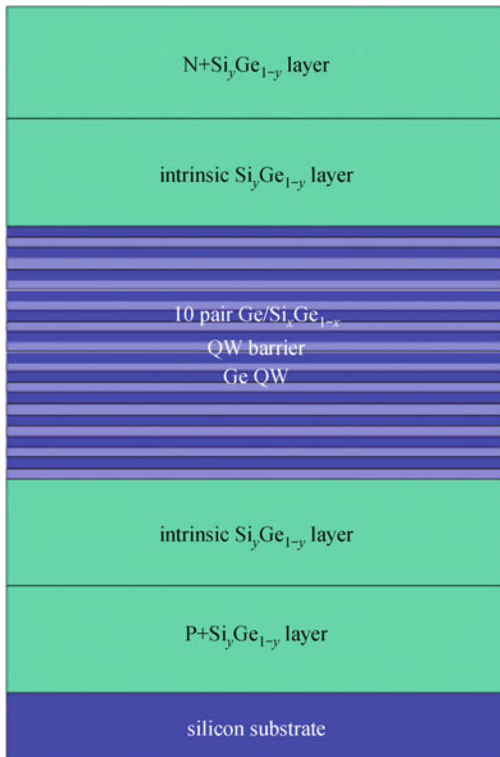

Fig. 1 A p-i-n structure on Si with Ge/$Si_{1-x}Ge_x$ QWs on relaxed $Si_{1-z}Ge_z$ buffer

Therefore, strong resonances corresponding to the heavy-hole and light-hole transitions are seen near the band-edge of the well material even at room temperature. When an E-field is applied across the QWs, it spatially separates the electrons and holes, reducing the overlap of their wavefunctions as well as the separation energy. This leads to both a red shift of the absorption and a decrease of the absorption intensity.

3 Device fabrication and experimental method

SiGe QW structure shown in Fig. 1 is grown in a commercial, reduced pressure chemical vapor deposition (RPCVD) reactor. It is a commercially available, cold-wall, single-wafer, mass-production tool and is routinely used in CMOS chip fabrication processes. The model used in this work is an Applied Materials Centura Epi Reactor with a "High Temperature Film" (HTF) chamber. The growth pressure capability of this reactor ranges from 1 to 600 Torr, the operating temperature capability ranges from 400°C to 1200°C.

In our work, we use direct deposition of p-doped SiGe buffers of the final SiGe composition on Si instead of the graded buffer method. The intrinsic SiGe spacer, the Ge QWs and the SiGe barriers are then deposited on top as an i-region. The thickness and composition of the barriers and wells are designed in a way that the QW superlattice is strain-balanced. Since the Ge well is compressively strained relative to the $Si_{1-z}Ge_z$ buffer, the $Si_{1-x}Ge_x$ barrier must be tensely strained ($x>z$) to compensate the compressive stress in the QW. The average Si concentration in the Ge/SiGe multiple quantum well (MQW) region is designed to be the same or similar to that in the buffer. The strain forces of the compressed Ge and extended SiGe layers of each QW pair cancel, and no net strain energy accumulates into the next pair. High Ge composition $Si_{0.1}Ge_{0.9}/Si_{0.15}Ge_{0.85}$ alloys are grown in the QW system. That material has very close physical properties and thermal mismatch strain can be neglected compared to lattice mismatch strain. Theoretically this would enable extension of the strained layer thickness beyond the critical thickness limitation to infinity.

The buffer layers are grown at 375°C for two cycles. For each cycle, 200 nm of SiGe is deposited and then annealed at 850ºC for 30 min. After two cycles, another SiGe intrinsic spacer with 100 nm is deposited. SiGe/Ge QWs are deposited at 375ºC as well. After that, another SiGe intrinsic spacer with 100 nm thickness is deposited. Finally, 200 nm of n-doped SiGe layer with the same Ge composition as the buffer layer is deposited as a cap layer. Before growth of each layer, the reactant gas flows were switched to "vent" for 40 s with only H_2 carrier gas flowing into the chamber to keep the gas flow steady. This will ensure all the QW interfaces are sharp and the Ge and

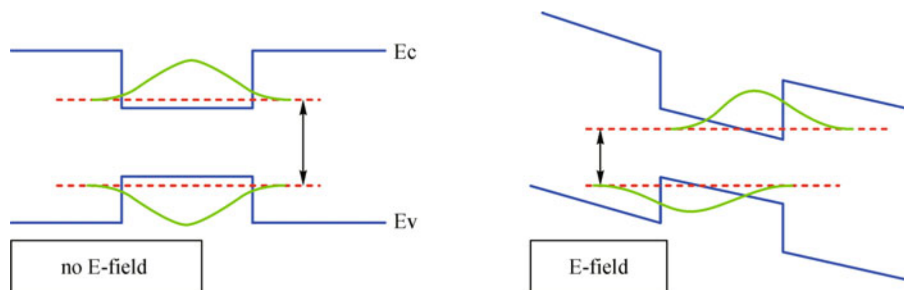

Fig. 2 QW conduction band and valence band energy (blue lines), carriers' wave functions (green lines) and energy states (red dash lines), and transition energy (arrows) with and without E-field influence

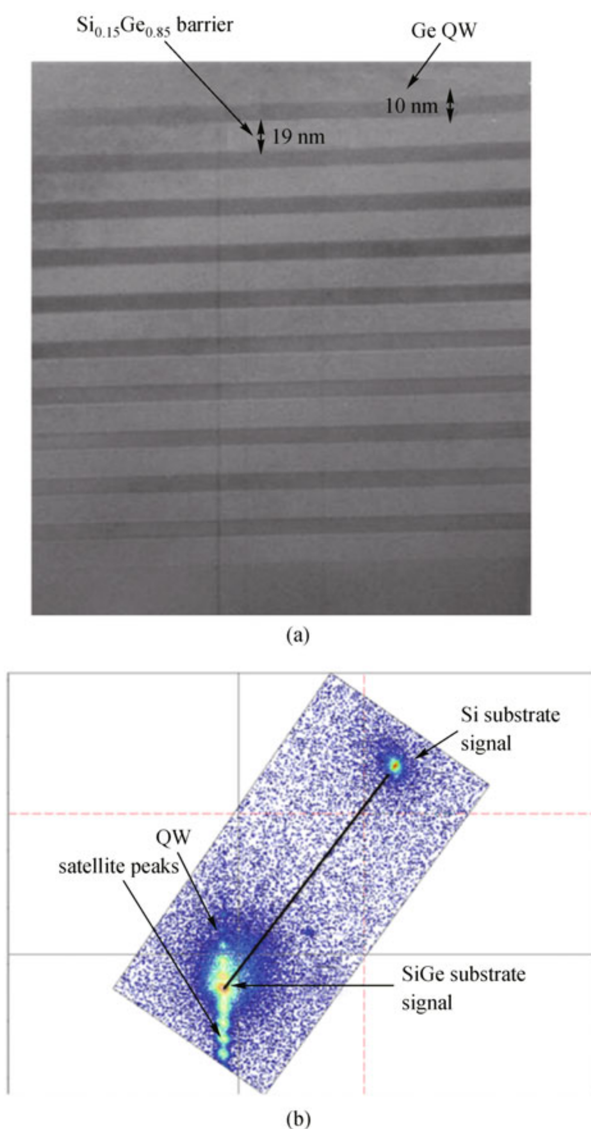

Fig. 3 (a) TEM cross section image of 10 pairs of Ge/SiGe MQW grown on Si; (b) 2D XRD reciprocal-space map of QW samples

doping profiles are sharp as well. The p-type buffer layer is boron doped with a doping level of about $5 \times 10^{18}\,cm^{-3}$, and the n-type cap layer is arsenic doped with a doping level of about $1 \times 10^{19}\,cm^{-3}$.

Figure 3(a) shows cross-sectional TEM image of 10 pairs of strained SiGe/Ge QWs grown on relaxed SiGe on Si. The Ge well is 10 nm and the $Si_{0.15}Ge_{0.85}$ barrier is 19 nm. The sharp and regular MQW structure provides steep barriers for better carrier confinement and improved optical quality. Figure 3(b) shows a 2D XRD reciprocal-space map of the MQW Ge/SiGe structure. The Si substrate signal and SiGe buffer layer signal are clear and sharp. The buffer peak is surrounded by several other peaks from the Ge/SiGe MQWs, which indicates a high MQW quality in this sample since it is difficult to observe that in SiGe/Si MQWs even when they are in the Si-rich end. Also, the line between SiGe and Si peaks is parallel to the omega-theta relaxation line, indicating that the buffer layer is fully relaxed. Also the satellite peaks indicate the SiGe/Ge QW structure is fully strained.

We started with this epitaxial growth recipe and fabricated devices with different mesa sizes (ranging from 5 μm × 5 μm to 500 μm × 500 μm) with standard complementary metal-oxide-semiconductor (CMOS) compatible processes. We also used the standard ground-signal-ground (GSG) probe configuration to couple the radio frequency (RF) signal to the devices.

Figure 4 shows the process flow of the high-speed optical modulator following the materials growth.

The first step (Fig. 4(b)) defines the two-level mesa. 1 μm thick photoresist (Shipley 3612) is spun for 30 s at 5000 r/min. A post bake of 120 s at 90ºC follows. A Karl Suss MA-6 aligner and standard optical lithography are used. Exposure time is 1.1 s. The wafer is then developed using LDD26W developer for 60 s. The first mask defines the upper mesa which extends down to the p-contact region. The second mask isolates the different devices by etching completely down to the Si substrate. Sulfur hexafluoride is used as the etchant. To better control the etch depth, a dummy wafer with the same epitaxial structure is etched to calibrate the etch rate immediately before etching the real devices.

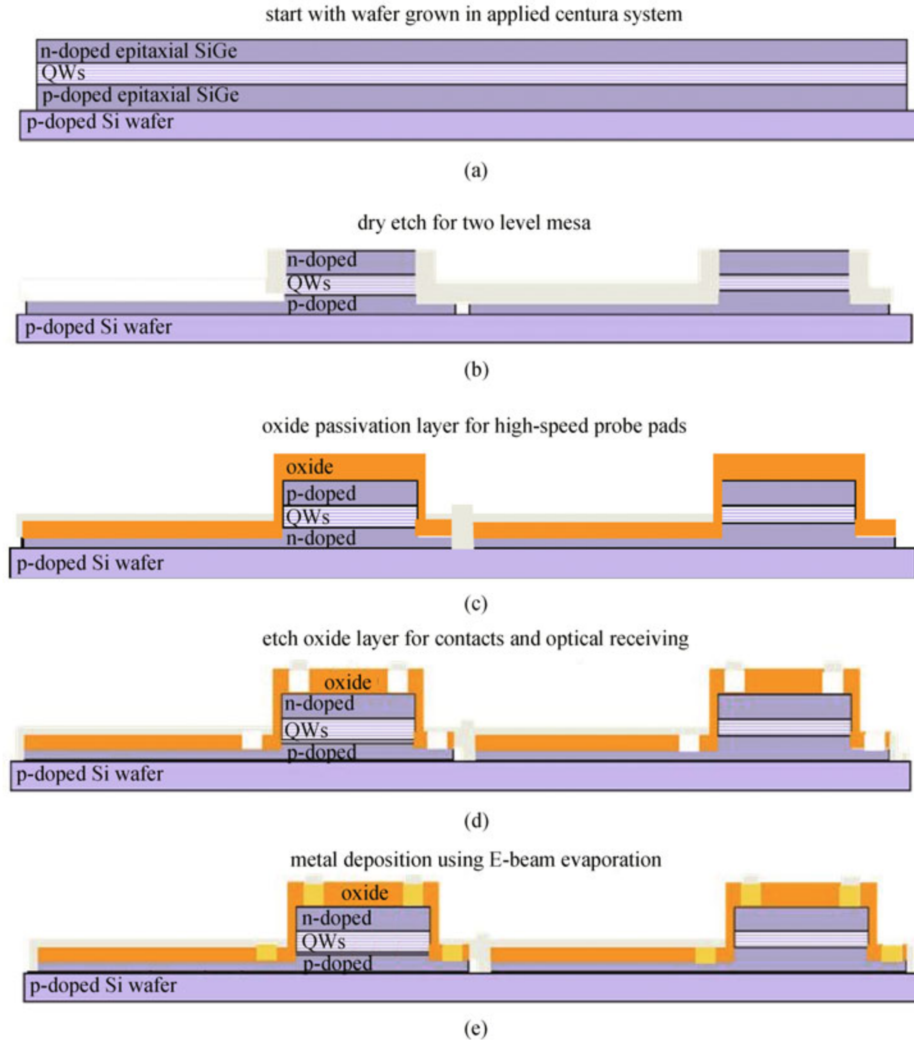

Fig. 4 High-speed modulator device process flow (a) epi wafer; (b) two mesa etch; (c) oxide passivation deposition; (d) double contact for p and n regions; (e) metal deposition for contacts

The second step is to deposit an oxide insulation layer using LPCVD to deposit a 600 nm thick Si dioxide layer at 400ºC for 30 min. The pressure is roughly 350 mTorr. Silane and oxygen are used in this process without phosphine doping.

The third step is back side oxide etching. We use 20∶1 buffered oxide etchant (BOE) to get better uniformity. The front side is covered by photoresist during this etch.

The fourth step is to pattern the optical window used for light input and to define the contact openings for transmission line evaporation. The mask process uses standard optical lithography, and the oxide is wet etched by 20∶1 BOE. The etching rate of undensified low-temperature oxide in 20∶1 BOE is 74 nm/min, and the oxide thickness is 600 nm in total. Since the wet etch is isotropic, and the side etch will potentially lead to a short circuit, the over etch must be less than 1 min. We control the etching by monitoring the residual oxide thickness every 2 min during the wet etch. We use a Nanospec film thickness measurement system, which is a non-contact, spectro-reflectometry tool that can measure transparent thin film thickness by processing the reflected light from the sample.

The fifth step is contact metallization. We use a metal liftoff approach by first using a mask to deposit photoresist to form a protection layer, then E-beam evaporating the contact metal over the patterned photoresist. 30 nm of titanium (Ti) and 1 μm of aluminum (Al) are deposited. Ti helps the metal adhere to the wafer while Al helps to produce reasonable contact coverage over the 3D transmission line structures. A 20 s hydrogen fluoride (HF) dip before metal evaporation is very important to achieve high-quality, low-resistance Ohmic contacts. Since the oxide opening is 600 nm deep, the contact metal has to be thick enough to get reliable metal coverage over the step at the edge of the oxide. After the evaporation, a standard metal lift-off process in an ultrasonic bath is used to remove the

resist and excess metal, leaving the desired contact pattern. After lift-off, the contacts are alloyed using rapid thermal annealing (RTA) at 375ºC for 30 s.

Figure 5 is an SEM picture of the completed device with coplanar microwave feed line. The mask pattern contains many devices of different sizes of squares, ranging from 100 μm down to 5 μm. We can clearly see the 3D structure of the metal contact, which can easily break at the edge between the SiGe and the oxide. The key for an effective contact is to ensure over etch of the oxide on SiGe before an adequately thick metal contact layer is subsequently deposited.

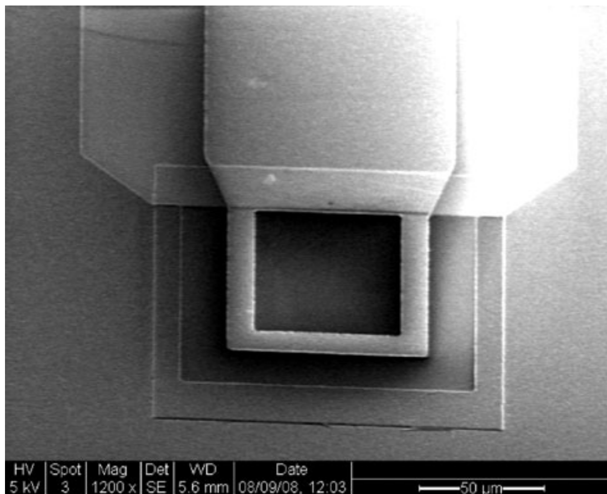

Fig. 5 SEM of the top view of the modulator

4 High speed characterization

4.1 Low-speed and high-speed E-O response

Figure 6 shows the absorption current spectra measured at room temperature for a structure with five Ge QWs, each 10 nm thick, separated by 15 nm thick, $Si_{0.13}Ge_{0.87}$ barriers, all grown on $Si_{0.1}Ge_{0.9}$ buffer layers. Note first that the spectra show clear exciton absorption peaks at room temperature. In bulk Ge, an exciton absorption peak can be seen at low temperature, but such peaks are not usually clearly resolvable at room temperature. The appearance of room temperature peaks is characteristic of the QWs, and is explained by the increased carrier confinement which maintains the excitons. At zero applied voltage, there is also a clear shift of the direct optical absorption edge from its value in the bulk, unstrained Ge (about 0.8 eV at room temperature) to the lowest energy exciton peak position of about 0.88 eV. This shift can be explained as a combination of strain and quantum confinement. The peaks and the shift show empirically that, despite the low indirect conduction band energy in the barriers relative to the well, there is a strong quantum confinement at the zone center in the Ge conduction and valence bands. When an E-field is applied, there is a clear QCSE shift of the absorption edge to lower photon energies.

In order to have strong enough optical modulation, a device with 20 pairs of QWs was used in our RF measurements. The AC response of different sized devices, ranging from 100 μm × 100 μm to 5 μm × 5 μm, was measured, and we found that the modulator performance is optimum at a DC bias of –2.5 V and an AC voltage swing of ±2 V. A 50 Ω resistor was used as the termination. The incident laser power is about 1 mW. We used two function generators; one which can generate square wave pulses up to 3.5 GHz, the second can generate sine waves up to 20 GHz.

Figure 7(a) shows the optical eye diagram of the modulator at 3.5 GHz. The laser output power is 1 mW, at a wavelength of 1408 nm. The operating characteristics and wavelength response have variations from device to device on the wafer, mostly due to non-uniformity of the device structure and materials induced during thin-film deposition and fabrication. Figure 7(b) shows the optical response to 10 GHz sine wave RF signal at a 40 μm device.

The diode dark current is at a level of 10 nA at low reverse bias with device size of 30 μm × 30 μm. At –5 V, the device reaches soft breakdown, and the dark current increases to 1 μA for the 100 μm device. However, the optical absorption current is always at 60 μW with 1 mW input power. The dark current can thus be neglected in the measurement.

For different size devices, measurements up to 3.5 GHz are performed and no major difference, in terms of optical response, is observed. With the 20 GHz function generator, a drop in response is observed for 100 μm devices at 3 GHz, and for the 30 μm devices, 10 GHz.

4.2 Pump/probe measurements

Figure 8 shows the pump probe measurement setup. The modulation bandwidth of the modulators was assessed using differential transmission spectroscopy (pump-probe) experiment. Pulses of about 350 fs width at about 1.4 μm were obtained from a Ti-sapphire pumped, optical parametric oscillator (OPO). The output of the OPO was split into three beams: a reference, a pump, and a probe. Acousto-optic modulators were used to shift the frequency of the probe and reference beams by 80 and 79 MHz, respectively. After propagation through the SiGe modulator with suitable delays, the probe and reference beams are overlapped on a slow detector. The amplitude of the difference frequency 1 MHz was detected using a high frequency lock-in amplifier. This signal is proportional to the transmission of the modulator. The energy of the pump and probe pulses was 650 and 20 fJ, respectively.

The response of the modulator depends strongly on the pump wavelength and bias voltage. Typically, the modulator transmission varies abruptly over a few

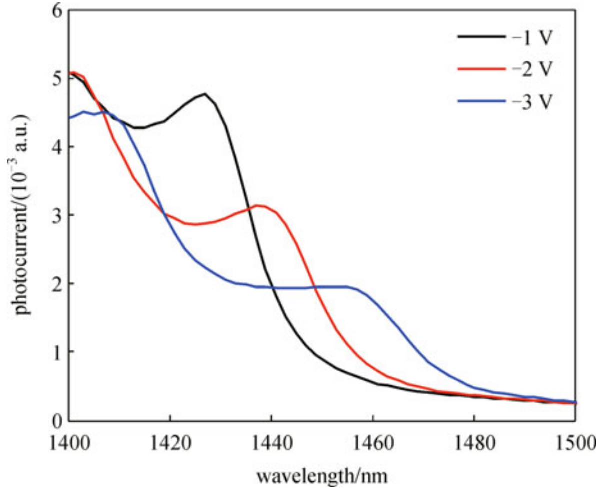

Fig. 6 Optical absorption current measurement

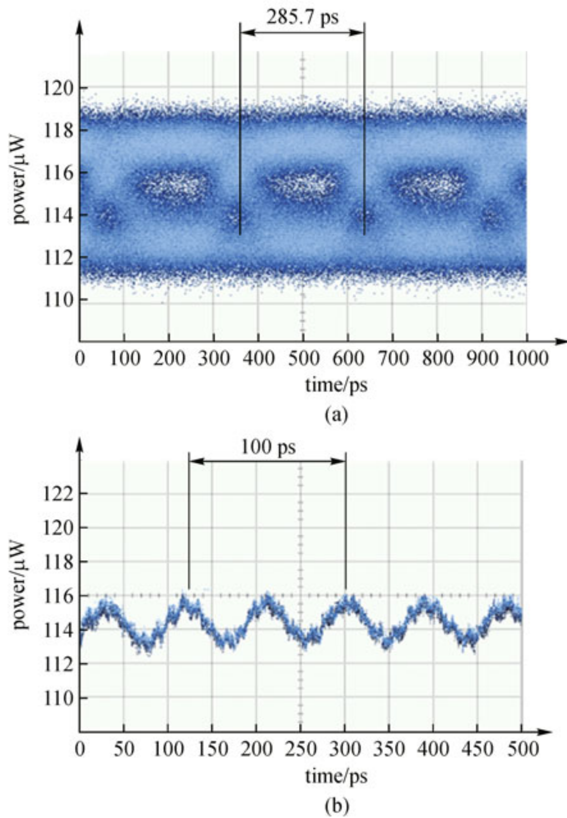

Fig. 7 (a) Optical eye diagram of 40 μm devices at 3.5 GHz; (b) optical response to 10 GHz sine wave RF signal

picoseconds and recovers to its initial transmission value within several tens of picoseconds. When the pump wavelength is fixed at 1.4 μm, the modulator exhibits a significant response for bias voltages larger than 4 V and the recovery time decreases with increasing bias.

Figure 9 shows the fitting curve of the carrier recovery time at wavelength of 1.4 μm. The fitting curves show that less than 6 V, the carrier lifetime is 44 ps and under 6.5 V it reduces to 30 ps. More results showed that at 11 V the lifetime is under 10 ps, indicating more than 100 GHz modulation capacity in the Ge/SiGe QW materials system.

4.3 Small signal measurement

The setup of the small signal measurement is very similar to that of the large signal electro-optical E-O response. The only difference is that the exciting optical signal is very small in amplitude and the response is collected and analyzed by a network analyzer.

Figure 10 shows the measurement results for the small signal E-O response under different biases. The wavelength of the input laser is tuned at 1420 nm, and the bias ranges from 2.5 to 5 V. The device size is 6 μm×6 μm.

It can be seen from the graph that the best optical response is obtained at 4 V of reverse bias. The modulation bandwidth can be roughly estimated at 10 GHz. This is reasonably consistent with rough estimation of the capacitance of the diode and the resistance of the test circuit.

There is an abrupt dip at 13 GHz, regardless of the bias voltage. The same behavior was observed in devices with different sizes ranging from 6 to 100 μm. This lack of dependence on device size is potentially due to the measurements being limited by the coupling of the high speed probe. Also, the resonant effect can be seen under different bias voltages. The most probable reason for this is high resistance in the N-contact. The metal Fermi level can possibly be pinned near the valence band maxima of Ge, making the contact behave more like a Schottky barrier contact instead of an Ohmic contact. This will create parasitic inductors and capacitors. In order to reduce these, the Ohmic contact must be improved, possibly by either Fermi level de-pinning in the N-type Ge or more heavily doping the Ge to produce a thinner barrier through which tunneling can occur.

5 Discussion

In this work, we demonstrated that because of the combined indirect and direct band gaps of Ge, very strong quantum confinement in the direct band gap can occur, but very fast tunneling into the lower indirect band gap makes Ge QW modulators potentially much faster than those fabricated in III-V materials because the carriers do not need to be thermally emitted out of the QW.

The pump-probe measurement shows that the Ge QW can potentially operate up to a modulation speed of 100 GHz with sufficiently high E-field intensity, but this is easily realized with a smaller number of QWs.

The small signal measurement results show the modulator $f_{3\ \mathrm{dB}}$ bandwidth greater than 10 GHz. Further study indicates that this can be even larger if the contact can be improved.

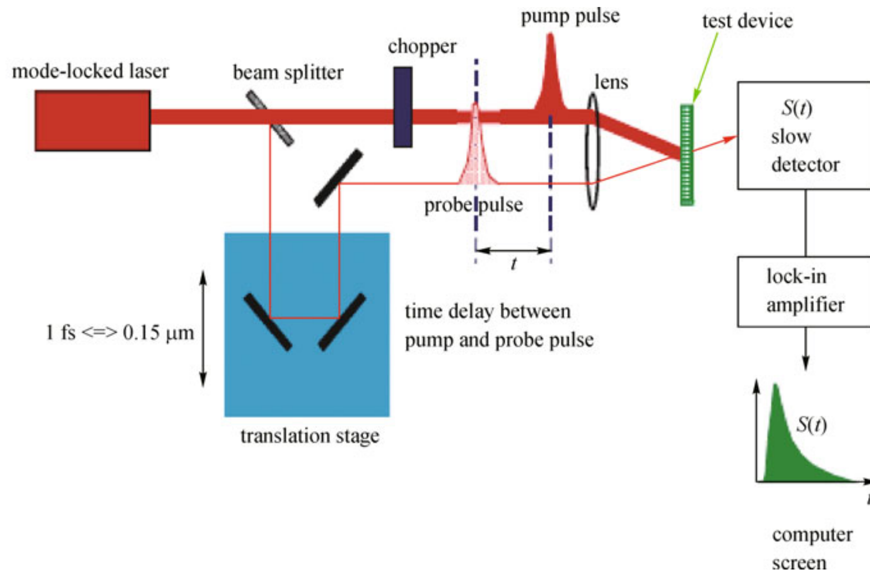

Fig. 8 Pump probe measurement setup

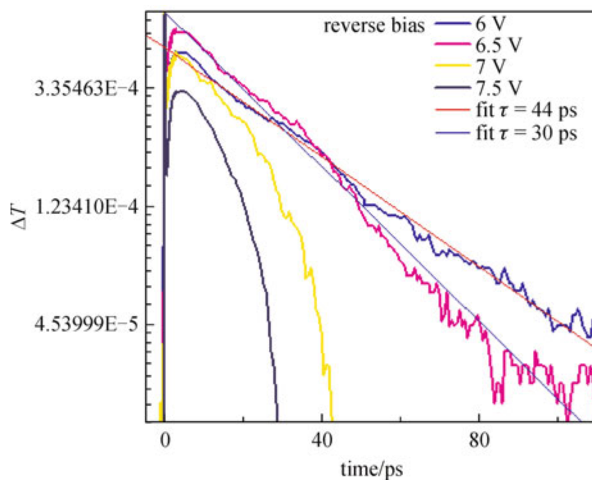

Fig. 9 Pump probe measurement result

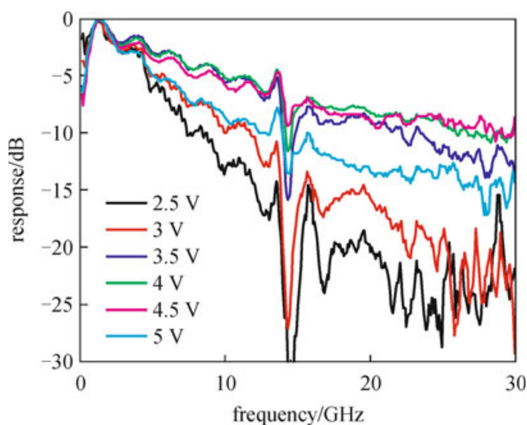

Fig. 10 Small signal measurement for 6 μm × 6 μm device

These results have been achieved on a first generation design and optimization of materials growth, device design and fabrication will certainly produce far better results in E-O response that could match the fundamental speed suggested in the pump-probe measurement.

6 Conclusions

We have demonstrated clear quantum confined Stark effect at the direct band gap of Ge in QWs with SiGe barriers. These devices utilize similar material structures compared to our previous work, but are grown in completely different deposition systems, thus demonstrating a technology that can be broadly developed in any of a number of epitaxial systems. Our measurement results prove the theoretical calculation of the absorption shift under different E-fields.

Also, based on the Ge QW material, we have fabricated coplanar high speed optical modulators. Optical measurements demonstrate a large signal E-O response. An eye diagram at 3.5 GHz and small signal optical modulation of up to 10 GHz were demonstrated. The pump probe measurement indicates that these devices have the potential to operate in the 100 GHz range, making these devices the most promising candidates for future high-speed optical interconnects.

The devices are fabricated using all CMOS standard processes, which make the devices reliable and suitable for CMOS integration. Also, the structure and the processes can be further optimized to achieve higher modulation and signal to noise ratio. One of the potentials of this Ge QW structure is that it can operate over a broad wavelength from operation at 1.3 μm by adding Si to the QW and designing thinner QWs to operation at 1.55 μm by combining strain and GeSn materials in the QW. This

will make these SiGe modulators attractive and compatible for both Si integrated circuits and optical networks.

To make faster and smaller devices in the future, we will focus on waveguide modulator structures, which can be as small as 1 μm × 1 μm in cross section and 20 μm long, yet still achieve a very high extinction ratio.

Acknowledgements The authors would like to thank Dr. E. Mohammed and Ian Young of Intel for support and for useful discussions and HP Labs in Palo Alto for access to their high-speed measurements facilities.

References

1. Miller D A B, Chemla D S, Damen T C, Gossard A C, Wiegmann W, Wood T H, Burrus C A. Band-edge electroabsorption in quantum well structures: the quantum-confined Stark effect. Physical Review Letters, 1984, 53(22): 2173–2177
2. Miller D A B, Chemla D S, Damen T C, Gossard A C, Wiegmann W, Wood T H, Burrus C A. Electric field dependence of optical absorption near the bandgap of quantum well structures. Physical Review B: Condensed Matter and Materials Physics, 1985, 32(2): 1043–1060
3. Lewen R, Irmscher S, Westergren U, Thylen L, Eriksson U. Segmented transmission-line electroabsorption modulators. Journal of Lightwave Technology, 2004, 22(1): 172–179
4. Arad U, Redmard E, Shamay M, Averboukh A, Levit S, Efron U. Development of a large high-performance 2-D array of GaAs-GaAs multiple quantum-well modulators. IEEE Photonics Technology Letters, 2003, 15(11): 1531–1533
5. Simes J, Yan R H, Geels R S, Coldren L A, English J H, Gossard A C, Lishan D G. Electrically tunable Fabry-Perot mirror using multiple quantum well index modulation. Applied Physics Letters, 1988, 53(8): 637–639
6. Lee Y H, Jewell J L, Walker S J, Tu C W, Harbison J P, Florez L T. Electrodispersive multiple quantum well modulator. Applied Physics Letters, 1988, 53(18): 1684–1686
7. Pezeshki B, Thomas D, Harris J S Jr. Optimization of modulation ratio and insertion loss in reflective electroabsorption modulators. Applied Physics Letters, 1990, 57(15): 1491–1493
8. Bar-Joseph I, Sucha G, Miller D A B, Chemla D S, Miller B I, Koren U. Self-electro-optic effect device and modulation convertor with InGaAs/InP multiple quantum wells. Applied Physics Letters, 1988, 52(4): 51–53
9. Goossen K W, Yan R H, Cunningham J E, Jan W Y. $Al_xGa_{1-x}As$-AIAs quantum well surface-normal electro absorption modulators operating at visible wavelengths. Applied Physics Letters, 1991, 59 (15): 1829–1831
10. Pezeshki B, Lord S M, Boykin T B, Shoop B L, Harris J S Jr. AlGaAs/AlAs QW Modulator for 6328 Å Operation. Electronics Letters, 1991, 27(21): 1971–1973
11. Kuo Y H, Lee Y K, Ge Y, Ren S, Roth J E, Kamins T I, Miller D A B, Harris J S. Strong quantum-confined Stark effect in germanium quantum-well structures on silicon. Nature, 2005, 437(7063): 1334–1336
12. Kuo Y H, Lee Y K, Ge Y S, Ren S, Roth J E, Kamins T I, Miller D A B, Harris J S. Quantum-confined stark effect in Ge/SiGe quantum wells on Si for optical modulators. IEEE Journal of Selected Topics in Quantum Electronics, 2006, 12(6): 1503–1513
13. Miller D A B. Rationale and challenges for optical interconnects to electronic chips. In: Proceedings of the IEEE, 2000, 88(6): 728–749
14. Kibar O, Van Blerkom D A, Fan C, Esener S C. Power minimization and technology comparisons for digital free-space ptoelectronic interconnections. Journal of Lightwave Technology, 1999, 17(4): 546–555
15. Cho H, Kapur P, Saraswat K C. Power comparison between high speed electrical and optical interconnects for interchip communication. Journal of Lightwave Technology, 2004, 22(9): 2021–2033
16. Park J S, Karunasiri R P G, Wang K L. Observation of large Stark shift in Ge_xSi_{1-x}/Si multiple quantum wells. Journal of Vacuum Science & Technology B Microelectronics and Nanometer Structures, 1990, 8(2): 217–220
17. MacFarlane G G, McLean T P, Quarrington J E, Roberts V. Fine structure in the absorption-edge spectrum of Ge. Physical Review, 1957, 108(6): 1377–1383
18. Dash W C, Newman R. Intrinsic optical absorption in single-crystal germanium and silicon at 77 K and 300 K. Physical Review, 1955, 99(4): 1151–1155
19. Kane E O. Band structure of indium antimonide. Journal of Physics and Chemistry of Solids, 1957, 1(4): 249–261